SAND2015-11110J

Topology Optimization with Cellular Structures

J. Robbins[1]

Multiscale Science: Sandia National Laboratories Albuquerque, NM, 87185

S.J. Owen, B.W. Clark

Simulation Modeling Sciences: Sandia National Laboratories Albuquerque, NM, 87185

T.E. Voth

Computational Multiphysics: Sandia National Laboratories Albuquerque, NM, 87185

Abstract

This paper presents an end-to-end design process for compliance minimization-based topological optimization of cellular structures through to the realization of a final printed product. Homogenization is used to derive properties representative of these structures through direct numerical simulation of unit cell models of the underlying periodic structure. The resulting homogenized properties are then used assuming uniform distribution of the cellular structure to compute the final macro-scale structure. A new method is then presented for generating an STL representation of the final optimized part that is suitable for printing on typical industrial machines. Quite fine cellular structures are shown to be possible using this method as compared to other approaches that use nurb based CAD representations of the geometry. Finally, results are presented that illustrate the fine-scale stresses developed in the final macro-scale optimized part and suggestions are made as to incorporate these features into the overall optimization process.

Keywords: additive manufacturing, cellular materials, homogenization, 3D printing, topological optimization

Email addresses: jrobbin@sandia.gov (J. Robbins), sjowen@sandia.gov (S.J. Owen), bwclark@sandia.gov (B.W. Clark), tevoth@sandia.gov (T.E. Voth)

[1]Sandia National Laboratories is a multi-program laboratory managed and operated by Sandia Corporation, a wholly owned subsidiary of Lockheed Martin Corporation, for the U.S. Department of Energy's National Nuclear Security Administration under contract DE-AC04-94AL85000.

1. Introduction

Interest in cellular materials continues to grow in light-weighting applications as technologies to realize these materials become more reliable, repeatable and of lower cost. Besides the weight savings inherent in these materials due to their low density (relative to the solid base material), cellular structures can also exhibit good dynamic performance, defect tolerance, corrosion and thermal resistance and lower cost than traditional materials [1, 2, 3].

Following the taxonomy of Wadley [4] cellular structures fall into one of two broad categories; stocastic and periodic. Stocastic structures are those where where the cellular structure is randomly distributed. While this cellular structure is among the easiest to manufacture using traditional techniques (e.g. foaming and sintering) its random layout and varying density make control of mechanical properties (and hence maximizing performance) difficult [4]. Better control of material properties are possible with periodic structures but their manufacture with traditional approaches is limited.

Periodic structures may also be amenable to numerical analysis at the scale of the part as homogenization techniques assume a regular or nearly regular structure at some scale [1]. Specifically, periodic cellular structures can be characterized by Representative Volume Elements (RVEs) that capture the repeatable structures evident in the material. When the RVE is of a size much smaller than the part they compose (i.e. "scale separation" exists) homogenization theory can be employed to provide representative material properties of the RVE that may be used to accurately describe the macro-scale response of the structure.

Although conventional manufacturing approaches are available and dominate the creation of these cellular materials, thier use becomes problematic for more complex cell geometries such as lattice structures [5]. These manufacturing limitations may be overcome by using Advanced Manufacturing (AM) techniques. Unlike traditional subtractive processes, AM approaches "print" parts from, for example, powders or droplets that are fused together with thermal or other process. In this way, AM can build parts that are otherwise unimaginable by traditional subtractive processes.

Approaches to multi-scale topological optimization can be broadly classified as concurrent and non-concurrent. In the non-concurrent approach either the structural (macro-structure) or micro-structure is optimized [5]. In the concurrent approach both macro- and micro-structure are "designed" together to get a final part [6]. In this paper we consider the non-concurrent approach, selecting a (spatially) uniform micro-structure and optimizing the macro-structure topology. Although the part design is based on the homogenized response we do examine the maximum total stresses (i.e. those that account for RVE stress raisers) in the final optimized geometries.

This paper begins with a discussion of homogenization theory and the application of homogenization to the linear elastostatic problem. This is followed by a description of the topological optimization algorithms use here. Note that a range of topological optimization algorithms are available for the compliance minimization problem including gradient-based methods such as Solid Isotropic with Penalization (SIMP), and level set techniques and evolutionary methods including the ESO and BESO approaches to name a few [7, 8]. Here we choose the SIMP approach and describe some of the important aspects of our implementation. This discussion is followed by a description of our process for mapping the optimized topology to a faceted representation that incorporates the cellular structure. This leads directly to an STL file that may be exported to a 3D printer for production without further user intervention. Finally we present results of our process to design realizable cellular parts and comment on the impact of stress risers due to the micro-scale features.

2. Problem Formulation

In the linear elastostatic setting, the expression for static equilibrium (conservation of momentum) is

$$\frac{\partial}{\partial x_j}\left(E^{\epsilon}_{ijkl}\left(\frac{\partial u^{\epsilon}_k}{\partial x_l}+\frac{\partial u^{\epsilon}_l}{\partial x_k}\right)\right)=0 \quad in\ \Omega \tag{1}$$

$$E^{\epsilon}_{ijkl}\left(\frac{\partial u^{\epsilon}_k}{\partial x_l}+\frac{\partial u^{\epsilon}_l}{\partial x_k}\right)\hat{n}_j=t^o_i \quad on\ \partial\Omega^t \tag{2}$$

$$u^{\epsilon}_i=u^o_i \quad on\ \partial\Omega^u \tag{3}$$

where t^o_i is the applied traction, u^o_i is the displacement constraint, $\hat{n}_i$ is the boundary surface normal, $\partial\Omega^u \cup \partial\Omega^t = \partial\Omega$, and $\partial\Omega$ is the boundary of the domain, Ω.

2.1. Homogenization

In periodic or nearly periodic heterogeneous materials the elasticity tensor, E^{ϵ}_{ijkl}, is assumed to vary with period of the structure, ϵ. The goal of homogenization is to (a) determine *effective* or *homogenized* material constants that account for this microscale variation, and (b) provide a means for examining the local or microscopic fields in component scale analysis [9, 1]. The approach begins with an asymptotic expansion of the dependent variable in the period of the structure, ϵ,

$$\mathbf{u}^{\epsilon}(\mathbf{x})=\mathbf{u}^0(\mathbf{x},\mathbf{x}/\epsilon)+\epsilon\mathbf{u}^1(\mathbf{x},\mathbf{x}/\epsilon)+\epsilon^2\mathbf{u}^2(\mathbf{x},\mathbf{x}/\epsilon)+... \tag{4}$$

The material response is assumed to be Y-periodic, where Y is the domain of the periodic cell. Recasting equation (1) in terms of the local variable, $\mathbf{y}=\mathbf{x}/\epsilon$, yields

$$\mathcal{A}^{\epsilon}_{ik}\mathbf{u}^{\epsilon}_k=0 \tag{5}$$

where $\mathcal{A}^{\epsilon}_{ik}$ is the differential operator:

$$\mathcal{A}^{\epsilon}_{ik}=\frac{\partial}{\partial x_j}\left(E^{\epsilon}_{ijkl}(\mathbf{y})\frac{\partial}{\partial x_l}\right). \tag{6}$$

Substituting in the expansion in equation (4) yields

$$\mathcal{A}^{\epsilon}_{ik}=\frac{1}{\epsilon^2}\mathcal{A}^1_{ik}+\frac{1}{\epsilon}\mathcal{A}^2_{ik}+\mathcal{A}^3_{ik} \tag{7}$$

in terms of the differential operators

$$\mathcal{A}^1_{ik}=\frac{\partial}{\partial y_j}\left(E^{\epsilon}_{ijkl}(\mathbf{y})\frac{\partial}{\partial y_l}\right) \tag{8}$$

$$\mathcal{A}^2_{ik}=\frac{\partial}{\partial y_j}\left(E^{\epsilon}_{ijkl}(\mathbf{y})\frac{\partial}{\partial x_l}\right)+\frac{\partial}{\partial x_j}\left(E^{\epsilon}_{ijkl}(\mathbf{y})\frac{\partial}{\partial y_l}\right) \tag{9}$$

$$\mathcal{A}^3_{ik}=\frac{\partial}{\partial x_i}\left(\mathcal{E}_{ij}(\mathbf{y})\frac{\partial}{\partial x_j}\right). \tag{10}$$

Equation (5) is satisfied if terms on powers of ϵ are equal to zero, i.e.,

$$\mathcal{A}^1\mathbf{u}^0 = 0 \tag{11}$$

$$\mathcal{A}^1\mathbf{u}^1 + \mathcal{A}^2\mathbf{u}^0 = 0 \tag{12}$$

$$\mathcal{A}^1\mathbf{u}^2 + \mathcal{A}^2\mathbf{u}^1 + \mathcal{A}^3\mathbf{u}^0 = 0. \tag{13}$$

Equations (11), (12), and (13) correspond to the lowest order terms, ϵ^{-2}, ϵ^{-1}, and ϵ^0, respectively. Since we are concerned with the limit as $\epsilon \to 0$, any higher order terms are neglected.

Equation (11) requires $\mathbf{u}_0$ be constant in $\mathbf{y}$, i.e., $\mathbf{u}^0 = \mathbf{u}^0(\mathbf{x})$, so equation (12) can be reduced to

$$\mathcal{A}^1_{ik}u^1_k = -\frac{\partial E^\epsilon_{ijkl}}{\partial y_j}\frac{\partial u^0_k}{\partial x_l}. \tag{14}$$

At this point we wish to find a solution for the microscale displacement, $\mathbf{u}^1$, to equation (14) that can then be used to reduce equation (13) to include only macroscale terms. The reduced form will define the homogenized problem that implicitly accounts for features at the microscale. To that end, we define the "cell problem" in the domain, Y, of the periodic cell to be

$$\mathcal{A}^1_{ij}\chi^{kl}_j = \frac{\partial E^\epsilon_{ijkl}}{\partial y_j} \tag{15}$$

where $\chi^{kl}_j(\mathbf{y})$ are Y-periodic. Combining the cell problem with equation (14) yields a solution for the fine scale:

$$u^1_i(\mathbf{x},\mathbf{y}) = -\chi^{kl}_i(\mathbf{y})\frac{\partial u^0_k}{\partial x_l} + \tilde{u}_i(\mathbf{x}) \tag{16}$$

where $\tilde{u}_i(\mathbf{x})$ is an arbitrary additive constant.

The solution, $\mathbf{u}^2$, to equation (13) exists only if the cell average of the forcing is zero [9], i.e.,

$$\int_Y \left(\mathcal{A}^2\mathbf{u}^1 + \mathcal{A}^3\mathbf{u}^0\right) d\mathbf{y} = 0. \tag{17}$$

Equations (16) and (17) reduce to a homogenized set of equations in terms of the macroscale, $\mathbf{u}^0$,

$$\frac{\partial}{\partial x_j}\left(H_{ijkl}\frac{\partial u^0_k}{\partial x_l}\right) = 0. \tag{18}$$

where the homogenized material properties, H_{ijkl}, are given by

$$H_{ijkl} = \left\langle E^\epsilon_{ijkl}\right\rangle - \left\langle E^\epsilon_{ijmn}\frac{\partial \chi^{kl}_m}{\partial y_n}\right\rangle. \tag{19}$$

In summary, the homogenized problem consists of the following:

Cell Problem (weak form):

$$\int_Y E^\epsilon_{ijkl}(y)\frac{\partial \chi^{kl}_m(y)}{\partial y_n}\frac{\partial v_i(y)}{\partial y_j}dY = \int_Y E^\epsilon_{ijmn}(y)\frac{\partial v_i(y)}{\partial y_j}dY \quad \forall\ v_i \tag{20}$$

Microscale Solution:

$$u^1_i = -\chi^{kl}_i(x,y)\frac{\partial u^0_k(x)}{\partial x_l} + \tilde{u}^1_i(x) \tag{21}$$

Effective Constants:

$$H_{ijkl} = \frac{1}{|Y|}\int_Y \left(E^\epsilon_{ijkl}(y) - E^\epsilon_{ijmn}(y)\frac{\partial \chi^{kl}_m}{\partial y_n}\right)dY \tag{22}$$

Homogenized System (weak form):

$$\int_\Omega H_{ijkl}\frac{\partial u^0_k(x)}{\partial x_l}\frac{\partial v_i(x)}{\partial x_j}d\Omega = \int_{\partial\Omega_t} t_i(x)v_i(x)d\Gamma \quad \forall\ v_i \tag{23}$$

2.2. Discretization

To solve the cell problems and homogenized system, the trial, characteristic, and test functions, u_i, χ^{jk}_i, and v_i, are approximated using a traditional Galerkin finite element discretization:

$$w^h_i(\xi) = \phi_I(\xi)w_{iI} \tag{24}$$

where $\phi_I(\xi)$ are basis functions defined in the parent coordinates, $\xi \in \Omega_\xi$, and w_{iI} are the discrete nodal values for the field of interest. The cell problems and homogenized systems are then:

Cell Problem (discrete form):

$$\mathbf{A}\boldsymbol{\chi}^K = \mathbf{B}^K \tag{25}$$

$$\mathbf{A} = \mathop{\mathsf{A}}_{el}\int_{\Omega_{\boldsymbol{\xi}}} \mathbf{B}^T_{el}\mathbf{E}^\epsilon(\mathbf{y}(\boldsymbol{\xi}))\mathbf{B}_{el}\det J^{el}_{\mathbf{y}\boldsymbol{\xi}}d\Omega \tag{26}$$

$$\mathbf{B} = \mathop{\mathsf{A}}_{el}\int_{\Omega_{\boldsymbol{\xi}}} \mathbf{B}^T_{el}\mathbf{E}^\epsilon(\mathbf{y}(\boldsymbol{\xi}))\det J^{el}_{\mathbf{y}\boldsymbol{\xi}}d\Omega \tag{27}$$

Effective Constants (discrete form):

$$\mathbf{H} = \frac{1}{|Y|} \sum_{el} \int_{\Omega_{\boldsymbol{\xi}}} (\mathbf{E}^{\epsilon}(\mathbf{y}(\boldsymbol{\xi})) - E^{\epsilon}(\mathbf{y}(\boldsymbol{\xi}))\mathbf{B}_{el}\boldsymbol{\chi}_{el}) \det J^{el}_{\mathbf{y}\boldsymbol{\xi}} d\Omega \tag{28}$$

Homogenized System (discrete form):

$$\mathbf{K}\boldsymbol{U} = \mathbf{F} \tag{29}$$

$$\mathbf{K} = \mathop{\mathsf{A}}_{el} \int_{\Omega_{\boldsymbol{\xi}}} \mathbf{B}^{T}_{el}\mathbf{H}\mathbf{B}_{el} \det J^{el}_{\mathbf{x}\boldsymbol{\xi}} d\Omega \tag{30}$$

$$\mathbf{F} = \mathop{\mathsf{A}}_{el} \int_{\Omega_{\boldsymbol{\xi}}} \mathbf{N}^{T}_{el}\mathbf{t}^{o} \det J^{el}_{\mathbf{x}\boldsymbol{\xi}} d\Omega \tag{31}$$

where, for element el, $\mathbf{B}_{el}$ is the symmetric gradient matrix, $\mathbf{N}_{el}$ is the nodal basis matrix, $\boldsymbol{\chi}_{el}$ is the matrix of characteristic displacement degrees of freedom, $\det J^{el}_{\mathbf{x}\boldsymbol{\xi}}$ is the Jacobian determinant of the mapping from global coordinates, $\mathbf{x} \in \Omega$, to parent coordinates, $\boldsymbol{\xi} \in \Omega_{\xi}$.

The solution proceedure begins by solving the cell problem once for each of the unique characteristic displacements, χ^{kl}. Due to symmetry there are six unique terms in 3D and three unique terms in 2D. Then the effective constants can be found and the homogenized system solved. The microscale solution can be evaluated if information at the fine scale is desired.

2.3. Structural Optimization

Here we consider the problem of minimizing the compliance under conditions of static equilibrium and a given mass/volume. Following Bendsøe [7] we have:

$$\min_{\rho} c(\rho) = \mathbf{U}^{T}\mathbf{F} \tag{32}$$

$$\text{s.t. } \mathbf{K}(\rho)\boldsymbol{U} = \mathbf{F} \tag{33}$$

$$V(\rho) = \int_{\Omega} \rho(\mathbf{x}) d\Omega = V_o \tag{34}$$

$$0 \leq \rho(\mathbf{x}) \leq 1 \tag{35}$$

where $\rho(\mathbf{x})$ is the design field that defines the topology – a value of zero/one indicating absence/presence of material, respectively. Here, the design field is supported as a nodal bi-linear (2D) or tri-linear (3D) Lagrange basis function, and filtering (described later) is used to stabilize the equal-order density and displacement

fields. To account for the evolving topology in the enforcement of the equilibrium constraint, the global stiffness matrix is scaled according to the SIMP method [10]:

$$\mathbf{K}(\rho) = \left[\rho_{min} + (1 - \rho_{min})\,\rho^p\right]\mathbf{K}_o \tag{36}$$

such that the design field can be zero in void regions, but the local stiffness is always nonzero to ensure acceptable conditioning of the global system. In equation (36), the penalty exponent ($p = 3$) is chosen to limit the appearance of intermediate densities in the design, and the initial (fully dense) stiffness, $\mathbf{K}_o$, is given by equation (30).

The design update scheme used in this work follows Bendsøe [7]:

$$z_I^{n+1} = \begin{cases} 0, & z_I^n B_I^\eta < 0 \\ 1, & z_I^n B_I^\eta > 1 \\ z_I^n B_I^\eta, & \text{otherwise} \end{cases} \qquad \text{(no sum on I)} \tag{37}$$

$$B_I^\eta = -\frac{1}{\lambda}\frac{\partial c/\partial z_I}{\partial V/\partial z_I}. \tag{38}$$

where z_I^{n+1} are the optimization degrees of freedom from which the nodal design values, ρ_I, are computed using a projection operation. Recursive bisection is used to find the value for λ that produces an updated design, z_I^{n+1}, satisfying the volume constraint.

The projection operation is used to prevent checkerboarding, control minimum feature size, and improve smoothness of the resulting design, and consists of a convolution of a local kernel, $h(\mathbf{x}, \mathbf{y})$, with the optimization variable, i.e.,:

$$\boldsymbol{\rho} = \mathbf{M}\mathbf{z}^{n+1} \tag{39}$$

$$\mathbf{M}_{IJ} = \frac{h(\mathbf{x}_I, \mathbf{x}_J)}{\sum_{J \in N_{IJ}} h(\mathbf{x}_I, \mathbf{x}_J)} \tag{40}$$

where $\mathbf{x}_I$ is the position of node I, $\mathbf{x}_J$ is the position of the Jth neighbor of node I, and N_{IJ} is the set of nodes within a given radius, r, of node I. The kernel function used for this work is $h(\mathbf{x}, \mathbf{y}) = r - |\mathbf{y} - \mathbf{x}|$. Note that treating the projection as a matrix operation simplifies the implementation of this approach for parallel computing.

The approach described above has been implemented in Albany [11] – a massively parallel multiphysics analysis package based on the Trilinos [12] library. Albany uses template based generic programming principles and automatic differentiation (AD) to simplify the construction of new objectives/constraints and associated gradients. Albany has been used to rapidly develop finite element application codes in diverse areas including ice sheet modeling [13], computational poromechanics [14], and quantum device design [15]. Albany and Trilinos are open-source and available at github.com.

3. Construction of Cellular Models

To construct a cellular model, we first generate a hexahedral mesh from an STL geometry representation produced from a topology optimization procedure of Section 2.3. This STL representation is constructed from this design field, ρ, using the Sculpt meshing tool [16]. Sculpt is a companion application to the Cubit Meshing and Geometry Toolkit [17] developed at Sandia. It is a parallel all-hex tool that utilizes an overlay grid procedure that is ideally suited to the organic shapes generated from topology optimization. The procedure begins by generating a three-dimensional Cartesian grid bounding the STL geometry, where cell sizes are representative of the target cellular dimensions. Volume fractions are then computed from ρ for each cell of the Cartesian grid. Figure 1(A) shows an example Cartesian grid of volume fractions where v_i is the volume fraction of the i^{th} material contained within each grid cell and $\sum v_i = 1.0$. Material interfaces are approximated using a procedure described in [16]. Grid nodes close to material interfaces are moved to the surfaces as shown in figure 1(B). Figure 1(C) then shows a layer of hexahedra inserted on both sides of the material interfaces by projecting othogonally from the local interface tangent plane. To improve mesh quality, a smoothing step is performed to improve both smoothness of the interface plains and the quality of the hexahedra as shown in figure 1(D).

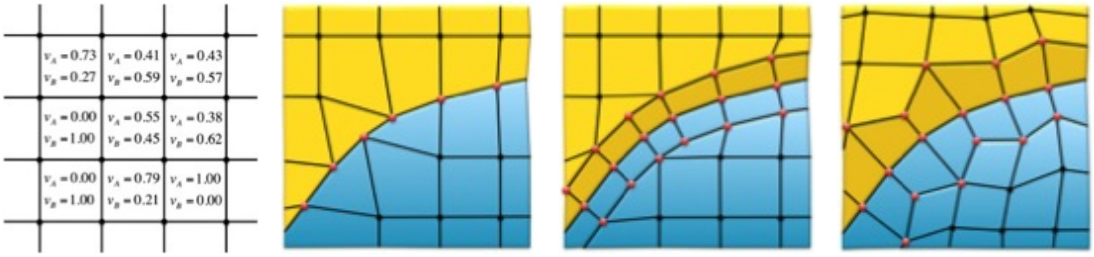

Figure 1: Sculpt procedure for generating an all-hex mesh.

Figure 2 illustrates a coarse hexahedral mesh generated from an STL geometry produced from a topology optimization procedure. Figure 2(A) is an exterior view of the mesh generated with Sculpt while (B) and (C) show cutaway views of the same. Note the regular interior structure of the mesh shown in (B) as well as the boundary conforming layer of hexes at the surfaces.

Having defined a hexahedral mesh, it can now serve as the structure on which a cylindrical lattice network can be defined. Within each hexahedra, a repeating geometry can be defined representing a single cell of the lattice network. While various configurations of lattice structures may be represented, we show three

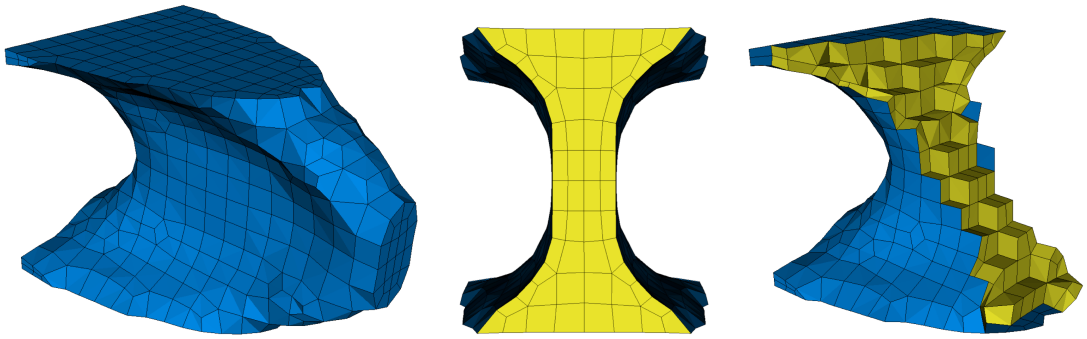

(a) (b) (c)

Figure 2: Example coarse hex mesh produced with Sculpt

examples of lattice geometry. Figure 3 shows solid model representations of hexahedron, octahedron and tetrahedon lattices. Note that the geometry for each of the lattice examples is symmetric around its three principal axis, a requirement to ensure the lattice geometry will be conforming between hexahedra.

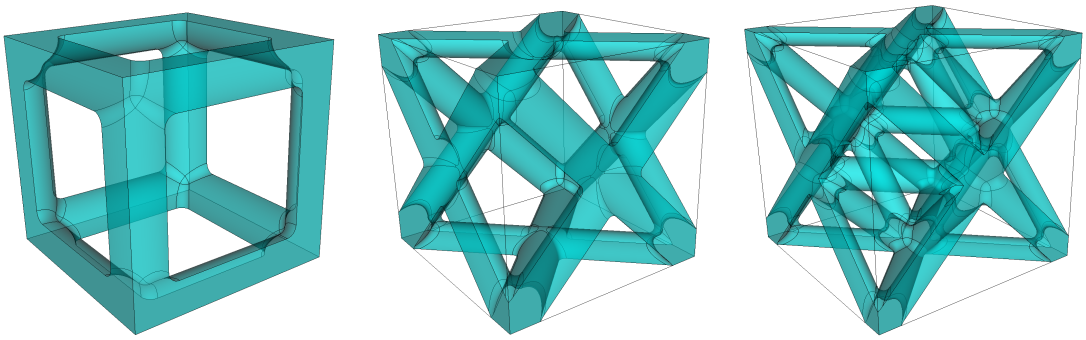

(a) (b) (c)

Figure 3: Solid model representations of lattice structures on a unit cube (A) Hexahedron, (B) Octahedron, (C) Tetrahedron

Although the solid model representation is convenient for visualization, it is impractical in application. Instead we simplify the lattice geometry into templates composed only of triangles that approximate the cylindrical lattice structures as shown in figure 4.

To build the lattice structure we copy the triangles of a given template into each hexahedron of the mesh. We note that the template triangles are defined on a unit cube, where x-y-z coordinate values are in the range 0.0 to 1.0. A local u-v-w parametric coordinate system can also be defined on a hexahedron with the same parametric coordinate range. A one-to-one mapping from the x-y-z coordinates

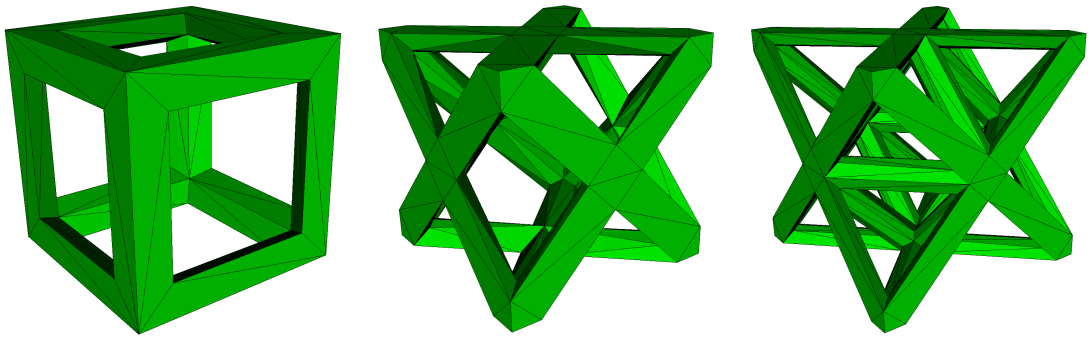

(a) (b) (c)

Figure 4: Simplified triangle representations of lattice structures on a unit cube (A) Hexahedron (96 triangles), (B) Octahedron (232 triangles), (C) Tetrahedron (468 triangles)

of the unit cube template to the u-v-w parametric space of the hexahedron can then be easily computed. To ensure a watertight volumetric representation of the lattice structure, triangles at the unit cube face boundaries are only copied when the corresponding hexahedral face is at a material boundary.

Figure 5 shows a simple example of a mesh of a sphere composed of 32 hexahedra. Lattice structures have been defined for each of the three different lattice configurations.

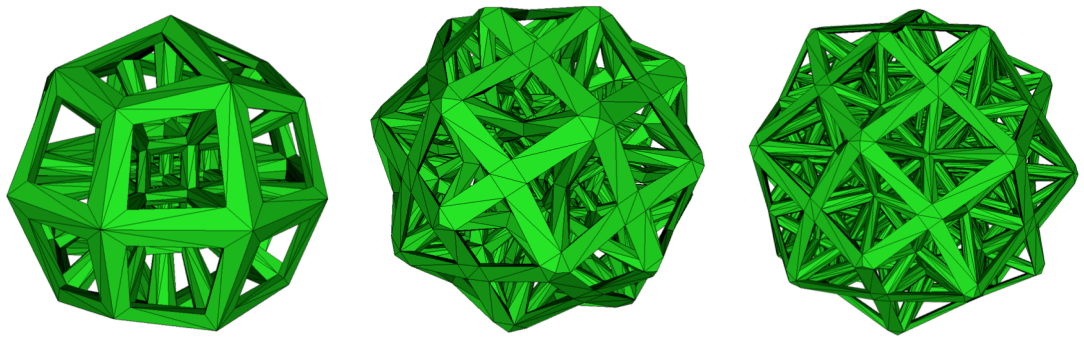

(a) (b) (c)

Figure 5: Lattice networks defined on a mesh of a sphere with 32 hexes (A) Hexahedron (1728 triangles), (B) Octahedron (5072 triangles), (C) Tetrahedron (12,624 triangles)

In the following section, this approach is shown to be a fast and reliable technique for creating complex cellular topologies.

4. Applications

4.1. Microstructured Materials

The homogenization proceedure described above can be used to account for microstructural effects in printed parts. Two microstructures are considered: a representative volume element (RVE) with a three-by-three array of elongated pores that are a) horizontally oriented (Figure 6) and b) vertically oriented. The Mitchell structure shown in Figure 7 is supported at the top and bottom corners of the left edge, and a vertical load is applied at the center of the right edge.

Problem setup requires a mesh for the RVE from which the characteristic solutions and effective material constants are computed, and a second mesh for conducting the optimization of the structure. Figure 6 shows paint plots of the three characteristic displacements that are computed in the initialization phase. These displacements are then used in equation (28) to compute the effective material stiffness, and the structural optimization proceeds based on the homogenized values.

The effect of the anisotropy that is introduced by the microstructure is evident in Figure 7. The material stiffness is greater in the direction parallel to the long axis of the pores. Depending on the orientation of the pores, the resulting optimized structure has tensile/compressive members that are oriented to take advantage of the directional stiffness.

The effect of heterogeneity on peak stresses can be considered by including the microscale solution in equation (21) to arrive at the *total* stress – the macro stress plus micro stress. The stress plots in Figure 7 show the average and maximum effective total stress for the two microstructures. As could be expected, the average effective total stresses are approximately the same as the effective macrostress. The maximum total stresses, i.e., the stresses that account for stress raisers in the RVE, are roughly twice the value of the average.

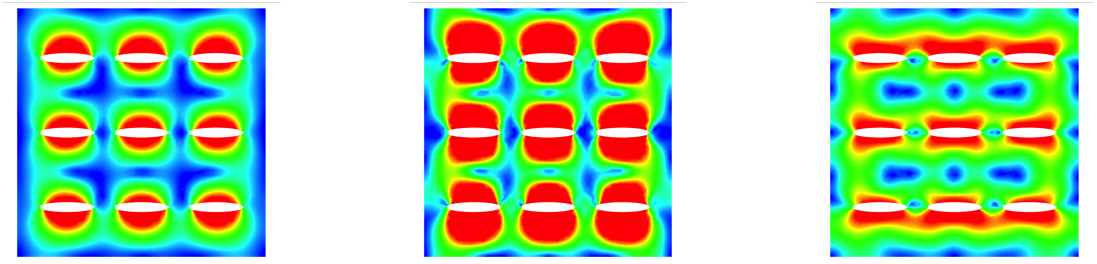

(a) Norm of χ^{xx} (b) Norm of χ^{yy} (c) Norm of χ^{xy}

Figure 6: Paint plots of the characteristic displacement fields.

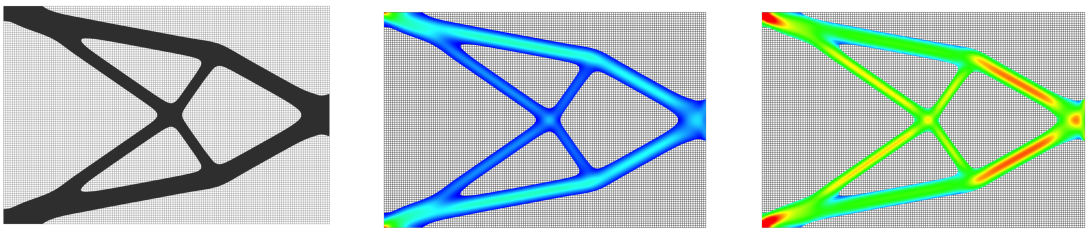

(a) Horizontal voids: Design (b) Average effective stress (c) Maximum effective stress

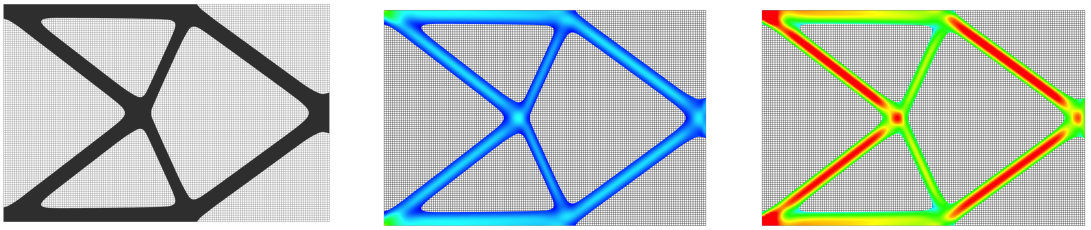

(d) Vertical voids: Design (e) Average effective stress (f) Maximum effective stress

Figure 7: Classic 2D Mitchell structure for horizontally oriented voids (top) and vertically oriented voids (bottom). Stress plot levels: Blue – 0.0 MPa, Red – 5.0 MPa.

4.2. Cellular Structures

Homogenization based topology optimization and subsequent construction of cellular models can be used to generate exceptionally lightweight and stiff structures. The approach is demonstrated in the context of a 3D Mitchell structure for which the RVEs and resulting optimized designs are shown in Figure 8. The designs correspond to the same cellular structure realized at four different material volume fractions: 10, 20, 50, and 75 percent of solid density (Figure 9).

The loading configuration consists of a fixed displacement on the left face with a vertical load applied to the center of the right face. The volume budget of each optimization is adjusted to maintain a constant mass among the designs. The design based on a fully dense material was given a volume budget of 6 percent of the design domain which results in volume budgets of 0.60, 0.30, 0.12, and 0.09 for cellular densities of 10, 20, 50, and 75 percent, respectively. The deflection at the load surface for the fully dense design is 6.1 mm, and the deflection (percent reduction) for the cellular designs is 2.5 mm (59%), 3.6 mm (41%), 5.4 mm (11%), and 5.7 mm (7%), for the 10, 20, 50, and 75 percent dense designs, respectively.

Figure 10 illustrates an example tetrahedron lattice structure for the mesh shown in figure 2. A close up view of the lattice structure is also shown in Figure 10(B) where the lattice structure for a single hexahadron in the mesh is highlighted. In this coarse mesh example, composed of 905 hexahedra, approximately 308,000 facets are generated. Also illustrated in figure 11 is a finer mesh representation

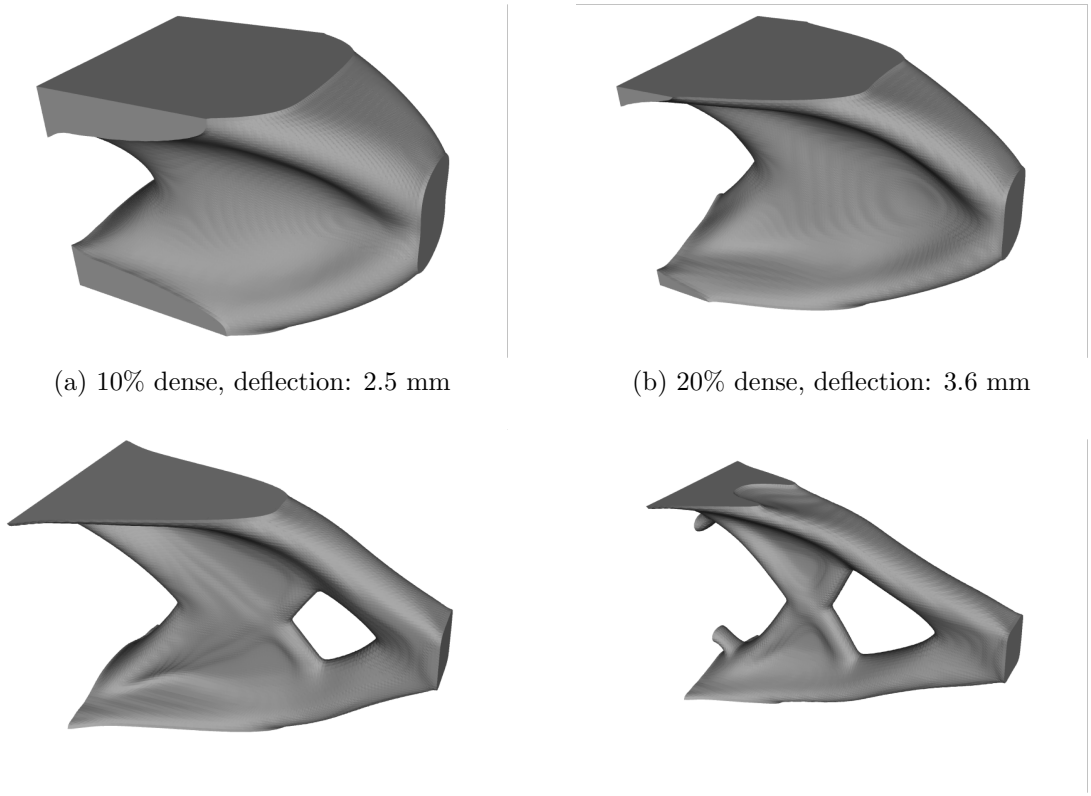

(a) 10% dense, deflection: 2.5 mm

(b) 20% dense, deflection: 3.6 mm

(c) 50% dense, deflection: 5.4 mm

(d) 75% dense, deflection: 5.7 mm

Figure 8: Fully dense design produces a deflection of 6.1 mm.

of the same model. In this example approximately 25 million facets have been generated. Time to generate the lattice structure geometry for this model was approximately 60 seconds or less.

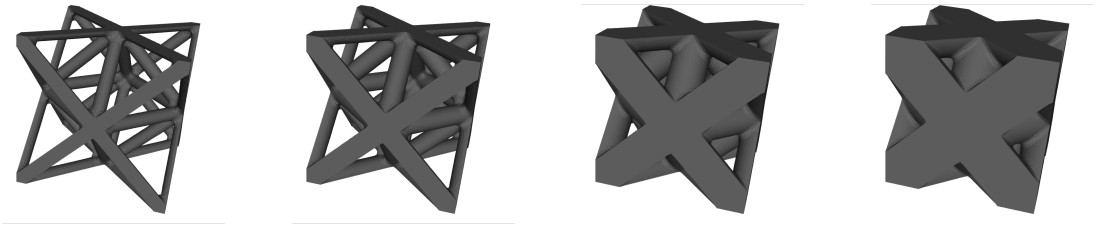

(a) 10% dense (b) 20% dense (c) 50% dense (d) 75% dense

Figure 9: Cellular structure with 10, 20, 50, and 75 percent density.

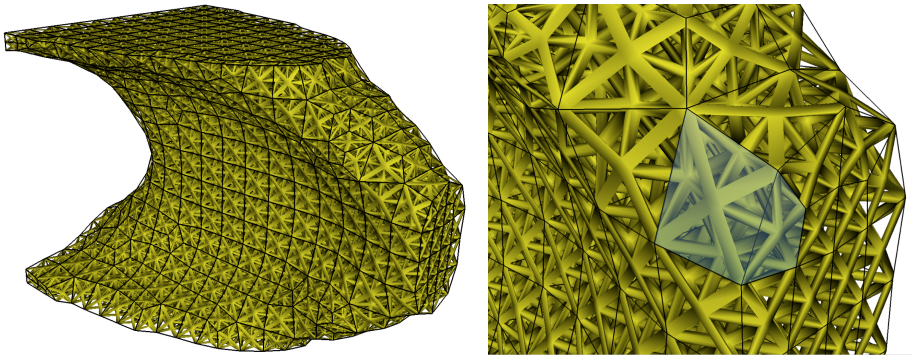

(a) (b)

Figure 10: Example tetrahedron lattice on a coarse mesh defined on a topology optimized geometry.

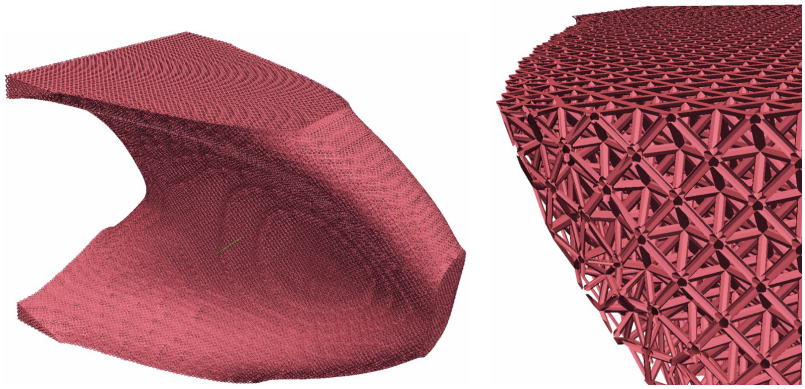

(a) (b)

Figure 11: Example tetrahedron lattice on a fine mesh defined on a topology optimized geometry.

5. Concluding Remarks

This paper presents an end-to-end design process for compliance minimization-based topological optimization of cellular structures through to the realization of a final printed product. Homogenization is used to derive properties representative of these structures through direct numerical simulation of unit cell models of the underlying periodic structure. It is seen that, as expected, part design is significantly impacted by cell micro-structure. Further we noted that stress-raisers are generated due to the micro-structure and these are not directly reflected in the part design. Specifically, a concurrent approach to the design that, for example, includes both compliance minimization as well as micro-scale stress minimization might be warranted. A methodology described here that maps the topologically optimized structure to a STL-ready representation is then used to contruct a printer-ready part. Resulting final designs are shown for moderate to fine cellular structures (relative to other related work). These micro-structured parts were then realized without further user intervention.

Acknowledgments: The authors would like to thank the members of the PLATO team at Sandia National Laboratories: Miguel Aguilo, Lauren Beghini, and Ted Blacker for valuable technical discussions and thorough review of the manuscript.

[1] B. Hassani and E. Hinton. A review of homogenization and topology optimization: I — homogenization theory for media with periodic structure. *Computers and Structures*, 69:707—717, 1998.

[2] E.W. Andrews and L.J. Gibson. The influence of cracks, notches and holes on the tensile strength of cellular solids. *Acta Materialia*, 49(15):2975—2979, 2001.

[3] Bin Niu, Jun Yan, and Gengdong Cheng. Optimum structure with homogeneous optimum cellular material for maximum fundamental frequency. *Structural and Multidisplinary Optimization*, 39:115—132, 2009.

[4] Haydn N.G. Wadley. Cellular metals manufacturing. *Advanced Engineering Materials*, 4(10):726—733, 2002.

[5] Pu Zhang, Jakub Toman, Yiqi Yu, Emre Biyikli, Mesut Kirca, Markus Chmielus, and Albert C. To. Efficient design-optimization of variable-density hexagonal cellular structure by additive manufacturing: theory and validation. *Journal of Manufacturing Science and Engineering*, 137:021004–1 — 021004–8, 2015.

[6] X. Yan, X. Huang, Y. Zha, and Y.M. Xie. Concurrent topology optimization of structures and their composite microstructures. *Computers and Structures*, 133:103—110, 2014.

[7] M.P. Bendsœand N. Kikuchi. Generating optimal topologies in structural design using a homogenization method. *Computer Methods in Applied Mechanics and Engineering*, 71(2):197—224, 1988.

[8] Ole Sigmund and Kurt Maute. Topology optimization approaches: A comparative review. *Structural and Multidisplinary Optimization*, 48:1031—1055, 2013.

[9] A. Benssousan, J.-L. Lions, and G. Papanicoulau. *Asymptotic analysis for periodic structures*. North Holland Pub. Co., Amsterdam, 1978.

[10] M.P. Bendsœ. Optimal shape design as a material distribution problem. *Structural and Multidisplinary Optimization*, 1:193—202, 1989.

[11] Albany, 2015. Available online at https://github.com/gahansen/Albany.

[12] Trilinos, 2015. Available online at http://trilinos.org.

[13] I. Tezaur, M. Perego, A. G. Salinger, R.S. Tuminaro, and S.F. Price. Albany/felix: a parallel, scalable and robust, finite element, first-order stokes approximation ice sheet solver built for advanced analysis. *Geoscientific Model Development*, 8:1197 – 1220, 2015.

[14] W. Sun, J.T. Ostien, and A.G. Salinger. A stabilized assumed deformation gradient finite element formulation for strongly coupled poromechanical simulations at finite strain. *International Journal for Numerical and Analytical Methods in Geomechanics*, 37:2755–2788, 2013.

[15] X. Gao, E. Nielsen, R. P. Muller, R.W. Young, A. G. Salinger, N.C. Bishop, M.P. Lilly, and M.S. Carroll. Quantum computer aided design simulation and optimization of semiconductor quantum dots. *Journal of Applied Physics*, 114, 2013.

[16] S. J. Owen, M. L. Staten, and M. C. Sorensen. Parallel hexahedral meshing from volume fractions. *Engineering with Computers*, 30(3):301—313, 2014.

[17] Cubit geometry and mesh generation toolkit, 2015.